Acta Pharmaceutica Sinica B 2018;8(3):390–400

Chinese Pharmaceutical Association
Institute of Materia Medica, Chinese Academy of Medical Sciences

Acta Pharmaceutica Sinica B

www.elsevier.com/locate/apsb
www.sciencedirect.com

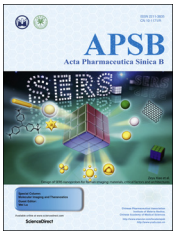

ORIGINAL ARTICLE

^{131}I-Evans blue: evaluation of necrosis targeting property and preliminary assessment of the mechanism in animal models

Qiaomei Jin[a,b,†], Xin Shan[c,†], Qi Luo[a,b,c], Dongjian Zhang[a,b], Yuanyu Zhao[c], Nan Yao[a,b], Fei Peng[a,b], Dejian Huang[a,b], Zhiqi Yin[c], Wei Liu[d,*], Jian Zhang[a,b,*]

[a]*Affiliated Hospital of Integrated Traditional Chinese and Western Medicine, Nanjing University of Chinese Medicine, Nanjing 210028, China*
[b]*Laboratories of Translational Medicine, Jiangsu Province Academy of Traditional Chinese Medicine, Nanjing 210028, China*
[c]*Department of Natural Medicinal Chemistry & Jiangsu Key Laboratory of Drug Screening, China Pharmaceutical University, Nanjing 210009, China*
[d]*Department of Nuclear Medicine, The First Affiliated Hospital of Nanjing Medical University, Nanjing 210029, China*

Received 16 May 2017; received in revised form 18 July 2017; accepted 5 August 2017

KEY WORDS

^{131}I-Evans blue;
Necrosis avidity;
Radioactivity;
DNA binding;
Necrosis imaging

Abstract Necrosis is a form of cell death, which is related to various serious diseases such as cardiovascular disease, cancer, and neurodegeneration. Necrosis-avid agents (NAAs) selectively accumulated in the necrotic tissues can be used for imaging and/or therapy of related diseases. The aim of this study was to preliminarily investigate necrosis avidity of ^{131}I-evans blue (^{131}I-EB) and its mechanism. The biodistribution of ^{131}I-EB at 24 h after intravenous administration showed that the radioactivity ratio of necrotic to viable tissue was 3.41 in the liver and 11.82 in the muscle as determined by γ counting in model rats. Autoradiography and histological staining displayed preferential uptake of ^{131}I-EB in necrotic tissues. *In vitro* nuclear extracts from necrotic cells exhibited 82.3% of the uptake in nuclei at 15 min, as well as 79.2% of the uptake at 2 h after ^{131}I-EB incubation. The DNA binding study demonstrated that evans blue

Abbreviations: CE-T1WI, contrast-enhanced T1WI; CT-DNA, calf-thymus DNA; DMSO, dimethylsulfoxide; DWI, diffusion-weighted imaging; EB, evans blue; H&E, haematoxylin-eosin; Hyp, hypericin; ^{131}I-EB, ^{131}I-evans blue; % ID/g, percentage of the injected dose per gram of tissue; MRI, magnetic resonance imaging; MPS, mononuclear phagocyte system; NAAs, necrosis-avid agents; PI, propidium iodide; RCP, radiochemical purity; RFA, radiofrequency ablation; RPLI, reperfused liver infarction; SD rats, Sprague–Dawley rats; T1WI, T1-weighted imaging; T2WI, T2-weighted imaging; TLC, thin layer chromatography

*Corresponding authors. Tel.: +86 25 68136549 (Wei Liu), +86 25 53262116 (Jian Zhang).
E-mail addresses: nuclearmedicine@163.com (Wei Liu), zhangjian@jsatcm.com (Jian Zhang).

†These authors made equal contributions to this work.

Peer review under responsibility of Institute of Materia Medica, Chinese Academy of Medical Sciences and Chinese Pharmaceutical Association.

http://dx.doi.org/10.1016/j.apsb.2017.08.002

(EB) has strong binding affinity with calf-thymus DNA (CT-DNA) (K_{sv} = 5.08×10^5 L/(mol/L)). Furthermore, the accumulation of ^{131}I-EB in necrotic muscle was efficiently blocked by an excess amount of unlabeled EB. In conclusion, ^{131}I-EB can not only detect necrosis by binding the DNA released from necrotic cells, but also image necrotic tissues generated from the disease clinically.

1. Introduction

Necrosis characterized by irreversible loss of plasma membrane integrity is a distinguished feature of many pathological conditions such as cancer, cardiovascular diseases, neurodegenerative disorders, autoimmune diseases and others[1]. And necrosis is also one of the major risk factors for accelerated deterioration of diseases[2,3]. The ongoing efforts have been put into understanding the role of cell necrosis in a range of diseases and therapeutics[4,5]. But to date, few appropriate cell necrosis imaging probes have been reported for clinical use in human.

Necrosis-avid agents (NAAs) which can selectively accumulate in the necrotic tissues are expected for both imaging and therapeutic applications[6,7]. Radiolabeled NAAs have been used as markers for noninvasive 'hot-spot imaging' to localize necrotic tissues such as myocardial infarction[8]. They provide a clear-cut distinction between viable and necrotic myocardium, which is crucial for myocardial viability determination and subsequent therapeutic decisions in clinical cardiology[9]. On the other hand, radioiodinated NAAs, which are preferentially taken up in tumor necrosis induced by antineoplastic drugs[10–12], emit radiation to kill and/or restrain adjacent residual cancer cells[13].

Porphyrin-based NAAs are still studied in preclinical experiments by different research centers[14,15]. Some porphyrin derivatives with superb necrosis targetability have been applied for visualization of necrosis including brain infarction and lesions of radiofrequency ablation (RFA). However, their clinical utility was limited by phototoxicity, unsatisfactory clinical tolerance and other potential side effects[16]. Hypericin (Hyp) has been recognized as one of the NAAs that exhibit a peculiar affinity for necrotic tissue. Nevertheless, Hyp is nearly insoluble in water and most nonpolar solvents, and shows unwanted retention in organs of the mononuclear phagocyte system (MPS)[17]. It will take a long time for Hyp to be used in clinical. Therefore, there is a pressing need for seeking safe and effective necrosis targeting probes with theragnostic purposes.

Evans blue (EB) is an artificial dye that may emit a bright red fluorescence as implied by its structure (Supplementary Information Fig. S1a)[18,19]. Interestingly, agricultural researchers apply EB staining to characterize maize endosperm cell death and identify key differences related to premature endosperm degeneration[20]. As a rapid and reproducible method, EB can stain damaged or dead cells in the plants[21,22]. In general, cell death in animals or in plants share many similar morphological and biochemical characteristics[23]. Moreover, EB has been used clinically as an intravenously injectable dye for determining the total blood volume in human, even in pregnant women and newborn babies, without adverse reactions[24,25]. Hence, we hypothesized that EB as a safety compound may exhibit necrosis targeting properties and could be applied for necrotic tissue imaging in animals.

The disruption of cytomembrane of necrotic cell results in the exposure of genomic DNA, which becomes the target of NAAs[26]. The previous study revealed that the planar-structured compounds have the potential to intercalate with double stranded DNA by forming stable complexes[27]. Therefore, we speculate that EB may target on the necrotic tissues by binding with DNA exposed on the necrotic cells.

In this study, necrosis targetability of ^{131}I-EB was evaluated by tissue γ counter, autoradiography, fluorescence microscopy and histochemical staining in rat reperfused liver infarction (RPLI). Nuclear extraction, fluorescence microscopy, DNA binding and blocking experiments were designed to examine EB necrosis targeting mechanism on cellular/tissue level.

2. Materials and methods

2.1. Materials and reagents

Sprague–Dawley rats (SD, male, 260–280 g) were provided by the Experimental Animal Center of Academy of Military Medical Sciences. All experimental protocols were approved by the Ethical Committee of Nanjing Drum Tower Hospital, the Affiliated Hospital of Nanjing University Medical School. The care and treatment of all animals were maintained in accordance with NIH publication No.85-23 (revised in 1996) on "Principles of laboratory animal care". EB was commercially available from Sigma Chemical Co. (St Louis, MO, USA) with purity greater than 98%. Sodium iodide's ($Na^{131}I$) radionuclidic purity was >99% and specific activity was 555 MBq/mL, which was supplied by HTA Co., Ltd. (Beijing, China).

2.2. Labelling of EB by ^{131}I

The iodogen coating method was conducted successfully in this study. Radioiodination was carried out by adding $Na^{131}I$ solutions and EB (1 mg/mL) (volume ratio, 1:4) into iodogen (1,2,4,6-tetrachloro-3α,6α-diphenylglycoluril; Sigma, St. Louis, MO, USA) tube (containing 100 μg of iodogen). The compound was shaken and incubated for 6.5 h at 70 °C, and terminated by removal of reaction solution. Radiochemical purity (RCP) of ^{131}I-EB was determined by thin layer chromatography (TLC).

2.3. *In vitro stability study of the radiotracer*

^{131}I-EB was incubated in rat serum (1:9 volume ratio) at 37 °C. At the time points of 0.5, 4 h, 1, 2, 3, and 8 day, respectively, the radiolabeling stability was determined by TLC.

2.4. *Animal models of necrosis*

All animals were given 0.1% potassium iodide in drinking water from 3 days before the experiment till the end of experiment to protect the thyroid gland from taking up free ^{131}I.

The models of RPLI and absolute ethanol induced muscular necrosis were prepared according to a previously introduced method[28,29].

RPLI model. SD rats ($n=23$) were anesthetized by intraperitoneal injection of chloral hydrate at a dose of 0.3 g/kg. Under laparotomy, reperfused liver infarction were induced by temporarily clamping the hilum of the right liver lobe for 3 h. After reperfusion by declamping hepatic inflow and by giving massage to the liver lobe, the abdominal cavity was closed with two-layer sutures.

Muscular necrosis model. Model rats of reperfused liver infarction and six health rats were intramuscularly injected with 0.2 mL absolute alcohol in the left leg to establish chemically induced muscular necrosis. All rat models were allowed to recover for at least 8 h after the procedure.

Detailed experimental procedures in the study are illustrated in Supplementary data Fig. S1b.

2.5. *Magnetic resonance imaging examination in vivo*

Magnetic resonance imaging (MRI) was used to determine whether or not the necrosis model was successful and to determine the dimension and location of necrosis. At 24 h, three rats with reperfused liver infarction and absolute ethanol induced muscular necrosis were anesthetized with isoflurane by using a small-animal gas anesthesia machine (Matrix VMP; GENE&I, Beijing, China), and placed in a wrist coil for MRI scanning at a 1.5 T whole body MRI scanner (GE, Milwaukee, WI, USA). MRI with T1-weighted imaging (T1WI), T2-weighted imaging (T2WI), diffusion-weighted imaging (DWI), and contrast-enhanced T1WI (CE-T1WI) sequences were performed, and gadolinium-based agent Magnevist (469.01 mg/mL, Bayer Schering Pharma AG, Berlin, Germany) was injected intravenously at 0.1 mL per rat for contrast enhancement.

2.6. *Tracer administration*

The model rats were injected with ^{131}I-EB (14.8 MBq/kg) dissolved in PBS solutions through a tail vein for biodistribution and targetability studies.

2.7. *Pharmacokinetics*

Six healthy rats were intravenously injected with ^{131}I-EB (14.8 MBq/kg) dissolved in PBS solutions. Then 10 μL blood were collected by slitting the tail at 5, 10, 30 min, 1, 2, 4, 6, 8, 12, 24 and 48 h, respectively. The radioactive counts of blood samples were measured with the automatic γ counter (WIZARD 2470; Perkin Elmer, Massachusetts, USA), and corrected for physical decay and background radiation. The results were calculated and expressed as MBq per liter.

2.8. *Radiobiodistribution, autoradiography and histopathological staining*

Twenty model rats with reperfused liver infarction and absolute ethanol induced muscular necrosis were allotted into experimental groups of four time points ($n=5$ each) by randomization. ^{131}I-EB formulation was intravenously injected through the tail vein under anesthesia, and model rats were sacrificed at 12, 24, 72 h and 8 day, respectively. Organs of interest (blood, brain, thyroid, lung, heart, spleen, kidney, stomach, pancreas, small intestine, large intestine, skeleton, skin, normal liver, necrotic liver, normal muscle and necrotic muscle) were dissected and weighed, and then radioactive counts of organs were measured using an automatic γ counter. Percentage of the injected dose per gram of tissue (%ID/g) was calculated. Corrections were made for physical decay and background radiation during counting.

The frozen necrotic/normal liver and partially necrotic muscle at each time point were cut at −20 °C into 30 μm serial sections with a cryotome (Shandon, Thermo Fisher Scientific, Waltham, MA, USA) and exposed 3 h to a high-performance storage phosphor screen (Cyclone; Canberra-Packard, Ontario, Canada). The screen was read using a Phosphor Imager Scanner (Cyclone; Canberra-Packard, Ontario, Canada) and digitally photographed with Optiquant software (Pacard, Packard Meriden, CT, USA). Afterwards, these sections were stained with haematoxylin-eosin (H&E) using the conventional procedure for co-localization of histological findings and autoradiography.

2.9. *Fluorescence microscopy*

Necrotic/normal liver and partially necrotic muscle was excised and cut into cryostat slices (5 μm). These slices were examined using a fluorescence microscopy equipped to acquire fluorescence images (AxioCam HR, Carl Zeiss, and Göttingen, Germany) with a light microscope using 200× magnifications in combination with computer-assisted image analysis software (Axiovision, Zeiss). For analysis, three measurements were performed for every destabilization time and mussel. Photomicrographs were taken under a bright or fluorescent field and subsequently the same sections were stained with H&E and photographed for comparison of detailed morphology. Fluorescence emission intensity was recorded at $\lambda_{ex}=620$ nm and $\lambda_{em}=680$ nm.

2.10. *Cell culture*

A human non-small cell lung cancer line A549 obtained from American Type Culture Collections (ATCC, Manassas, VA, USA) were subcultured in RPMI-1640 medium supplemented with 10% calf serum, penicillin (100 U/mL) and streptomycin (100 μg/mL) in a 5% CO_2 atmosphere at 37 °C. All reagents for cell culture were obtained from KeyGEN Biotech (Nanjing, China).

2.11. *Flow cytometry*

The percentage of necrotic cells was estimated by staining with annexin V-FITC/propidium iodide (PI) kit (Becton Dickinson, Franklin Lakes, NJ, USA). A549 cells at a concentration of 1×10^6 cell/mL were incubated under intense hyperthermia (57 °C) for 1 h

to induce necrosis. A549 cells without hyperthermia treatment were used as a control. The cells were analyzed on a FACSCalibur benchtop flow cytometer and data were acquired with Cell Quest acquisition software, version 3.3 (Becton Dickinson Biosciences, San Jose, California). All fluorescence measurements were made on a four-decade log scale.

2.12. *Nuclear extraction and fluorescence microscopy experiment*

A549 necrotic and viable cells were incubated with ^{131}I-EB (50 μmol/L) for 15 min and 12 h at room temperature. Nuclear extracts were prepared by using a nuclear extraction kit (KGA826 , KeyGEN Biotech, Nanjing, China) according to the manufacturer's instruction. The radioactive counts of nuclear and other components were measured with the automatic γ counter.

Fluorescence microscopy used to demonstrate the performance of EB in necrosis and viable cells. A549 cells were seeded (5×10^4/well) in a 12-well plate (Corning lnc., Corning, New York, USA) supplemented with RPMI-1640 medium containing 10% calf serum. Necrosis was induced by above-mentioned method for 1 h. Necrosis and viable cells were incubated with EB (50 μmol/L) for 30 min at room temperature, and then, EB was replaced with 500 μL of PBS solution plus and 5 μL of 50 μg/mL PI (red fluorescence) and 10 μL of 1 mg/mL Hoechst 33342 (blue fluorescence, Becton Dickinson, Franklin Lakes, NJ, USA), and cells were incubated for 20 min. PI only stains the nuclei of necrotic cells and Hoechst 33342 stain both viable cell and necrotic cell nuclei. The cells were immediately visualized by using a Zeiss Axio Observer (AxioCam HR, Carl Zeiss, and Göttingen, Germany) with a light microscope using 400 × magnifications in combination with computer-assisted image analysis software (Axiovision, Zeiss). Observed at 488/617 nm excitation and 350/461 nm of PI and Hoechst 33342 excitation/emission wavelength under the microscope. For analysis, three measurements were performed for every destabilization time and mussel.

2.13. *Interaction with calf-thymus DNA*

Calf-thymus DNA (CT-DNA, Sigma, St. Louis, MO, USA) solution were prepared by dilution of CT-DNA to Tris-HCl buffer (5 mmol/L Tris-HCl/50 mmol/L NaCl buffer, pH 7.4) followed by exhaustive stirring at 4 °C for three days. The solution of CT-DNA gave a ratio of UV absorbance was determined by Cary 5000 spectrophotometer (Varian, Australia) at 260 and 280 nm (A_{260}/A_{280}) of 1.8:1–1.9:1, indicating that the CT-DNA was sufficiently free of protein. The concentration of CT-DNA was determined by the UV absorbance after 1:10 dilution using $\varepsilon = 6600$ L/mol.cm at 260 nm[30].

2.14. *Competitive study with ethidium bromide*

The competitive studies of EB with ethidium bromide (well-known DNA intercalating agent) have been investigated with fluorescence spectroscopy was determined by Cary eclipse fluorescence spectrophotometer (Agilent Technologies) in order to examine whether the compound can displace ethidium bromide from CT-DNA-ethidium bromide complex. Due to strong intercalation between the adjacent DNA base pairs, ethidium bromide emits intense fluorescence light in the presence of CT-DNA[34]. The fluorescence spectra ($\lambda_{ex} = 530$ nm, $\lambda_{em} = 604$ nm) were recorded at 25 °C and EB solution with original concentration of 6.0×10^{-4} mol/L were added into 2.5 mL CT-DNA-ethidium bromide solution (CT-DNA = 6.0×10^{-5} mol/L) to get the concentration ratio of EB/CT-DNA-ethidium bromide varying from 0 to 7/30 respectively. The relative binding ability of the compound with CT-DNA was determined by classical Stern–Volmer equation [31].

$$I_0/I = 1 + K_{sv}[\text{compound}] \quad (1)$$

where I_0 and I are the fluorescence intensity in absence and presence of the quencher, K_{sv} is the Stern–Volmer quenching constant, and [compound] is the concentration of the EB.

2.15. *UV–vis spectroscopic studies*

The interaction of EB with CT-DNA has been studied with UV–vis spectra in order to investigate the possible binding modes to CT-DNA. Increasing concentrations CT-DNA was micropipetted directly into a 1.0 cm cell containing 1.0×10^6 mol/L EB (total volume 2.5 mL), and the reaction was performed at 25 °C. The synchronous UV–vis spectra were recorded by scanning both 480–720 nm wavelengths simultaneously.

2.16. *Self-blocking experiment*

Rats model of muscular necrotic ($n = 3$ for each group) were intravenously *via* the tail vein with approximately 3.7 MBq

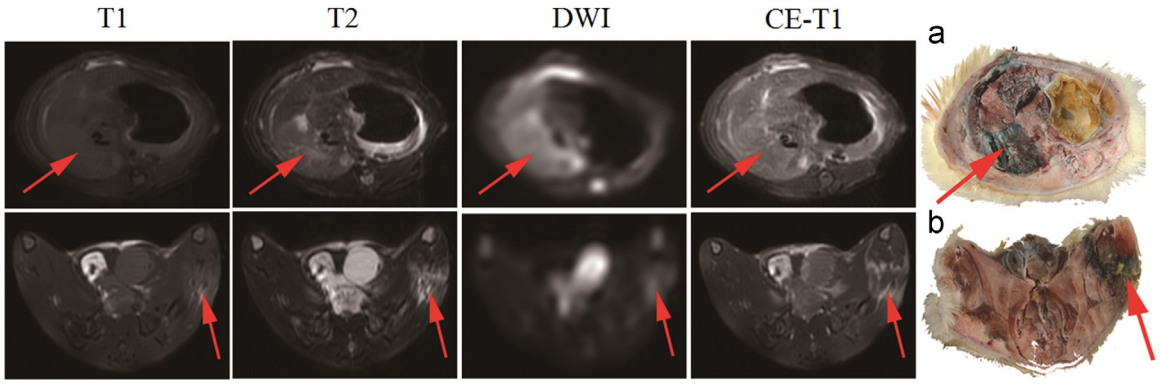

Figure 1 The rat *in vivo* MRI images of necrosis in reperfused liver infarction and muscle necrosis models. The first row was T1WI, T2WI, DWI and CE-T1WI weighted MR images and macroscopic photographs with the necrosis liver lobe (arrow) and the second row was that of muscle necrosis area (arrow). The liver lobe with reperfused liver and necrotic muscle appeared higher signal on T2WI, DWI and CE-T1WI images. Evens blue appeared blue uptake in the infarcted right liver lobe (a) and necrotic muscle (b), indicated by arrows. ($n = 3$).

(100 μCi) of ^{131}I-EB with or without ~10 mg/kg of EB and then was sacrificed at 24 h. Tissues of interest were weighed and the radioactivity was measured with a γ-counter. Corrections were made for background radiation and physical decay. The results were presented as percentage of the injected dose per gram of tissues (%ID/g). And then, the tissue were cut at −20 °C into 30 μm serial sections with a cryotome and exposed 6 h to a high-performance storage phosphor screen. The screen was read using a Phosphor Imager scanner and digitally photographed with Optiquant software. Afterwards, these sections were stained with H&E using the conventional procedure for co-localization of histological findings and autoradiography. These slices were examined using a fluorescence microscopy equipped to acquire using a Zeiss Axio Observer with a light microscope using 200× magnifications in combination with computer-assisted image analysis software. For analysis, three measurements were performed for every destabilization time and mussel.

2.17. Statistical analysis

Quantitative data were averaged by groups and expressed as mean ± standard deviation. Pharmacokinetic parameters were determined by using Drug and Statistics for windows 2.0 software, SPSS Inc., Chicago, IL, USA. Between-group or data from tissues of interest were compared by one-way analysis of variance using Student's *t*-test and $P<0.05$ was considered statistically significant.

Table 1 Pharmacokinetic parameters of ^{131}I-EB dissolved in PBS solutions after i.v. administration at 14.8 MBq/kg in normal rats.

Parameter	Unit	Value for normal rat
AUC_{0-t}	MBq/L·h	564.82 ± 27.55
$AUC_{0-\infty}$	MBq/L·h	737.28 ± 62.32
$t_{1/2z}$	h	24.40 ± 3.64
T_{max}	h	0.083 ± 0
CLz	L/h/kg	0.021 ± 0.004
C_{max}	MBq/L	96.84 ± 10.05

AUC_{0-t} and $AUC_{0-\infty}$, area under the curve; $t_{1/2z}$, elimination half-life; T_{max}, peak time; CLz, clearance; C_{max}, peak concentration. The values are expressed as mean ± SD, $n = 6$.

3. Results

3.1. Radiolabeling and in vitro stability study

The radiolabeling method was simple and successfully conducted in this study. Radiolabeling yields were >95% for ^{131}I-EB as determined by TLC analysis (Supplementary information Fig. S2). *In vitro* stability of ^{131}I-EB stored in rat serum at 37 °C was over 90% up to 8 days.

3.2. Magnetic resonance imaging examination

As proven by *in vivo* MRI, RPLI and muscle necrosis models were successfully established for this experiment as seen in Fig. 1. The necrotic liver lobes appeared homogeneously isointense on T1WI, and hyperintense on T2WI, DWI and CE-T1WI images relative to the normal liver. The necrotic tissue in the left hind leg showed slightly hyperintense on T1WI and hyperintense on T2WI, DWI and CE-T1WI images compared to the healthy leg. EB stained infarcted liver lobes and necrotic muscle in dark blue, indicating special affinity for necrosis as shown by gross section (Fig. 1a and b).

3.3. Pharmacokinetics

The concentration–time curve of blood from 0 to 48 h was illustrated in Supplementary information Fig. S3. Pharmacokinetics parameters determined by non-compartmental model were summarized in Table 1. In normal rats, $t_{1/2z}$ of ^{131}I-EB was 24.40 ± 3.64 h after i.v. injection. The long half-life could facilitate delivering a high concentration of ^{131}I-EB into the necrotic area.

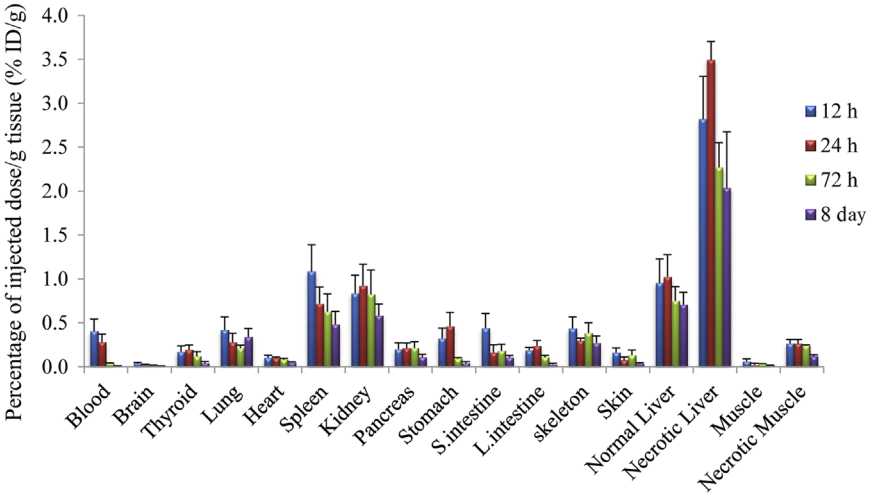

Figure 2 Biodistribution of ^{131}I-EB studies in reperfused liver infarction with muscle necrosis rats as a function of time ($n=5$, each time point). The injection dose of ^{131}I-EB is 14.8 MBq/kg, 2.0 mg/kg. Data are expressed as percentage injected dose per gram of tissue (% ID/g) ± SD. ($n=20$).

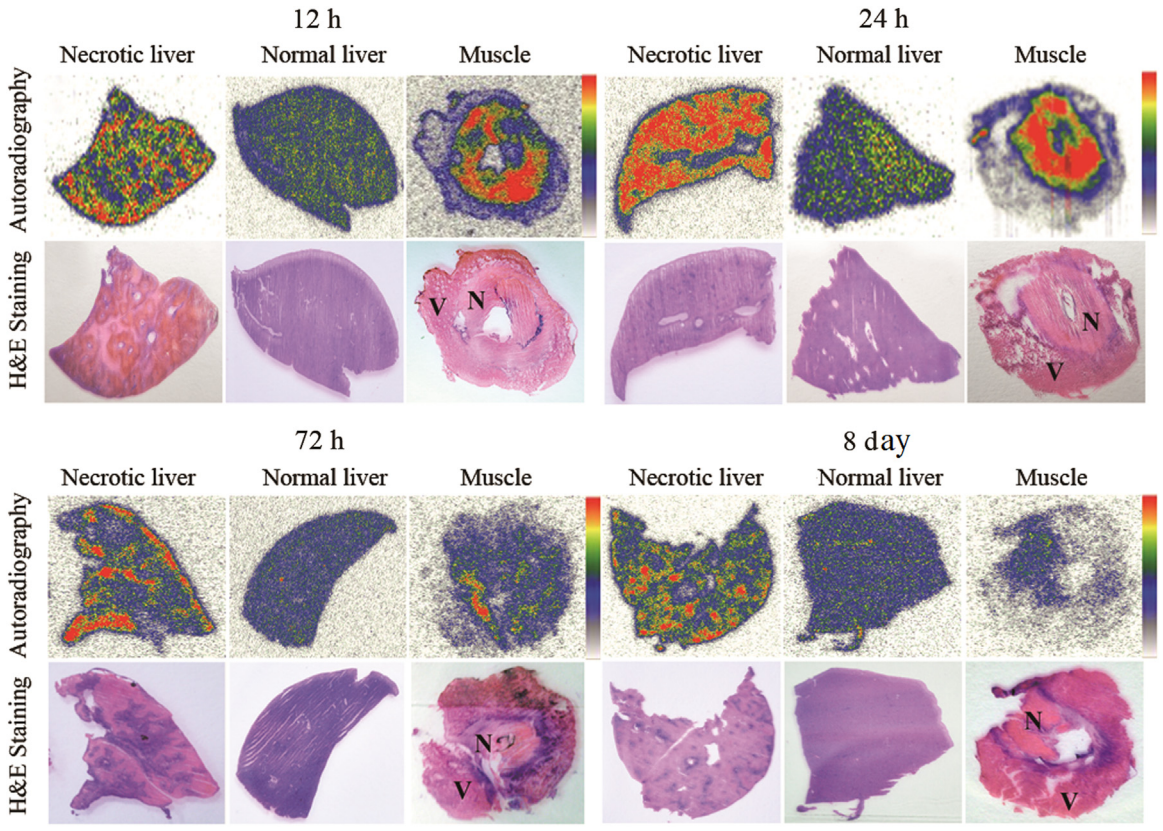

Figure 3 Autoradiograph and corresponding contrast-enhanced H&E images of 30 μm necrosis liver (left), normal liver (middle) and partially necrosis muscle (right) slices at 12, 24, 72 h and 8 days after i.v. injection of ^{131}I-EB (14.8 MBq/kg). The upper images were taken from autoradiography. The red parts were regions of high tracer uptake and the blue and yellow parts were regions with lower tracer uptake. The under images were taken from H&E stained sections. The dark purple regions were viable area (V) and the light pink parts were necrotic area (N).

3.4. *Biodistribution*

Fig. 2 exhibits biodistribution data after administration of ^{131}I-EB at different time points. The radioactivity reached their highest values at 12 h and significantly reduced with time after administration in normal tissue, especially in normal liver, spleen, and kidney. ^{131}I-EB uptakes in necrotic liver and muscle reached the highest level at 24 h. The data indicate that radioactivity within necrotic tissues maintained at relatively steady levels from 24 h to 8 days. The target efficiency or the ratios of necrotic liver and muscle over normal liver and muscle was 3.41 and 11.82 at 24 h, respectively. We observed that the accumulated radioactivity decreased more slowly in necrotic tissue than normal organs. Even at 8th day, the ratio of uptakes in the necrotic muscle was still 7.43 times higher than in the normal muscle.

3.5. *Autoradiography*

Fig. 3 shows the images of autoradiography and stained histopathology slices of necrotic and normal liver and partially necrotic muscle. Low tracer uptake is found in the haematoxylinophilic healthy liver (purple colored on H&E staining), whereas high tracer uptake appeared in the eosinophilic necrotic parts (pink colored on H&E staining). Consisting with the biodistribution results, these findings indicate that ^{131}I-EB mainly retained in the necrotic region. Determined by autoradiography at 24 h after intravenous injection of ^{131}I-EB, radioactivity ratios of necrotic to normal tissue amounted up to 4.26 and 10.2 in the liver and muscle, respectively.

3.6. *Fluorescence microscopy*

Selective retention of EB in necrotic tissues up to 8 days was demonstrated by fluorescence microscopy as shown in Fig. 4. The topographic distribution of the fluorescence intensity matches with that of the necrotic tissue distinguished by H&E staining. High fluorescence intensity appears only in the necrotic tissue, whereas low fluorescence intensity is found in the viable tissue.

3.7. *Analysis of necrosis by flow cytometry in vitro*

The targeting performance of EB in dying cells was tested with A549 cells. Hyperthermia treatment successfully induced necrosis of A549 cells. Flow cytometry demonstrated that untreated A549 cells (control cells) showed 4.12% of necrosis. Under 57 °C hyperthermia condition, the percentage of necrotic cells was 64.75% (Fig. 5).

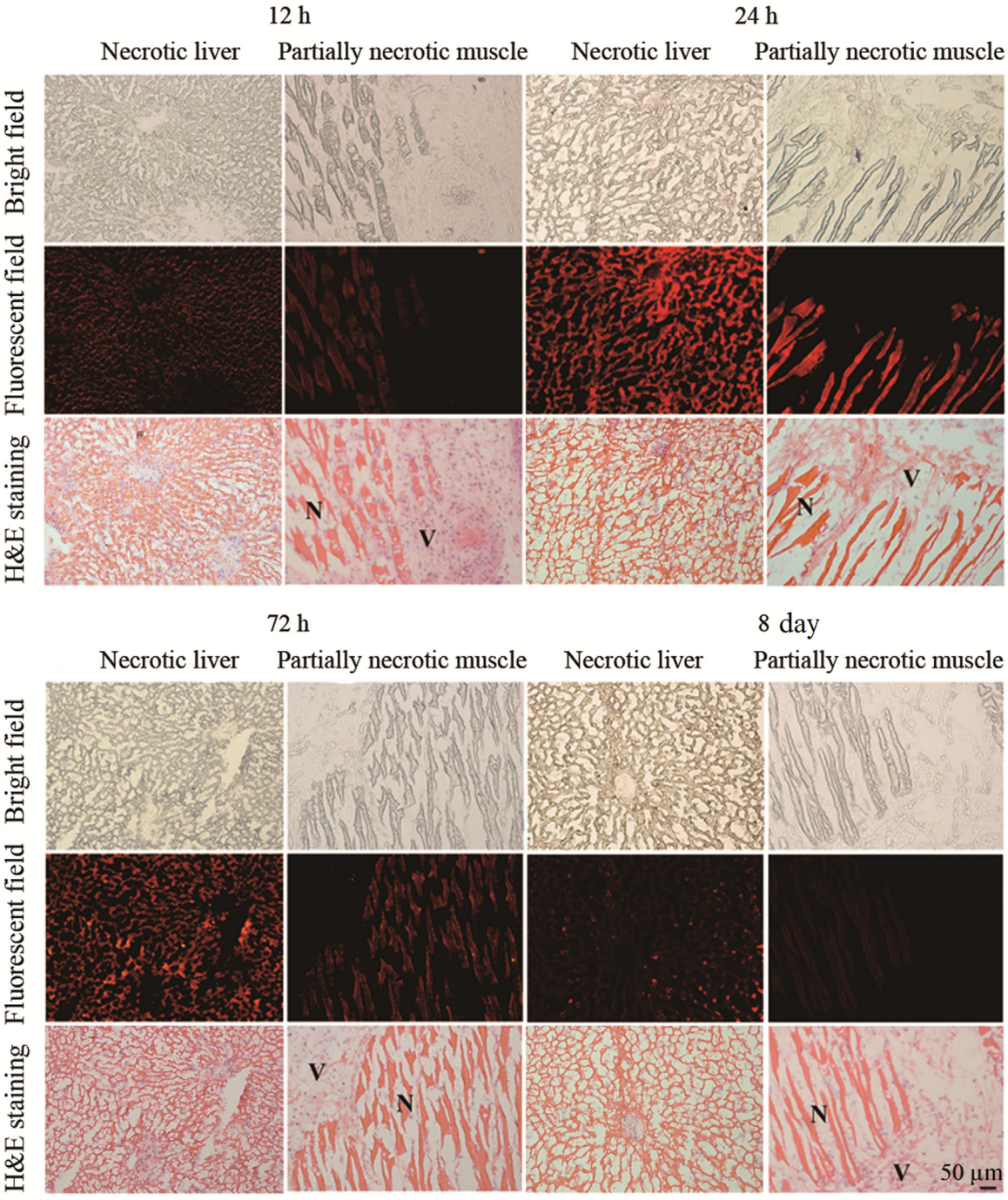

Figure 4 Photomicrography of 5 μm frozen liver slices containing reperfused liver (left) and muscle slices containing absolute ethanol induced necrosis (right) from the model rats at 12, 24, 72 h and 8 days after intravenous injection of EB (2.0 mg/kg), respectively. Fluorescence emission intensity was recorded at λ_{ex} = 620 nm and λ_{em} = 680 nm. Corresponding unstained (upper), fluorescence (middle) and H&E stained (under) pictures: N = necrotic area, V = viable area. Scale bar = 50 μm.

3.8. Nuclear extraction and fluorescence microscopy experiment

Nuclear extraction indicated that the uptake of EB in necrotic cell nuclei were 82.3% and 79.2% *in vitro* at 15 min and 2 h. Fluorescence microscopy was employed to trace distribution of EB in the necrotic and viable A549 cells (Fig. 5). The necrotic cells were co-stained with nuclear dyes (Hoechst 33342 and PI) before incubated with EB (bottom row). Viable cells were not stained with EB and PI (top row). The co-localization images suggested that EB was specifically located in the nuclei of necrotic cell.

3.9. DNA binding study using fluorescence and UV–vis spectroscopy

Fluorescent emission study of CT-DNA-ethidium bromide in the absence and presence of EB was shown in Fig. 6. As the

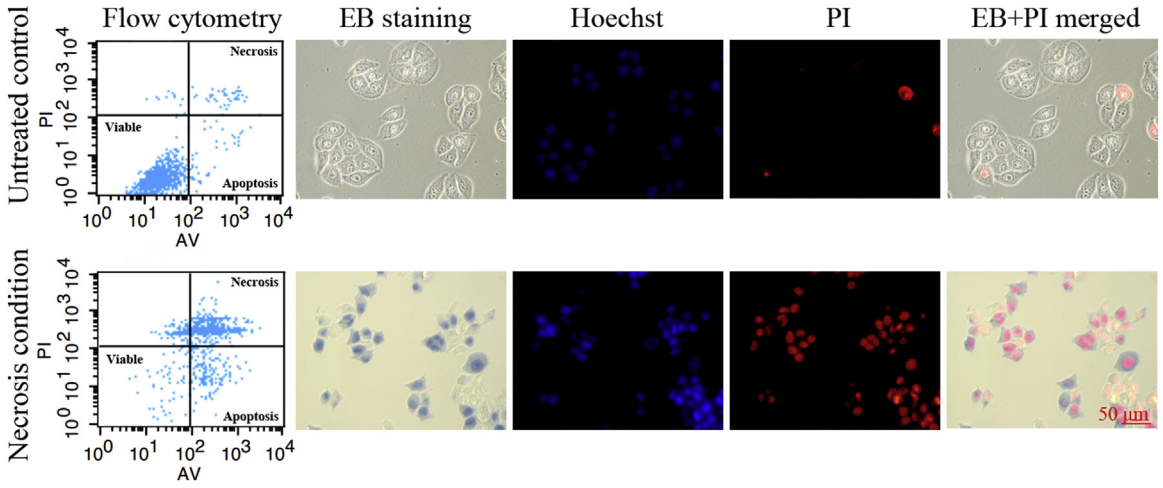

Figure 5 After co-staining with Annexin V-FITC and PI, untreated cells and necrosis cells were analyzed by flow cytometry to measure the percentage of necrotic cells. Necrotic cells were on the upper right gate and viable cells were on the lower left gate. Fluorescence microphotographs were acquired with necrotic cells and untreated cells after stain with EB, Hoechst 33342 and PI. EB were mainly situated in the cytoplasmic membrane of viable cells (top row) and were mainly located in the nucleus region of necrotic cells (bottom row). Scale bar = 50 μm.

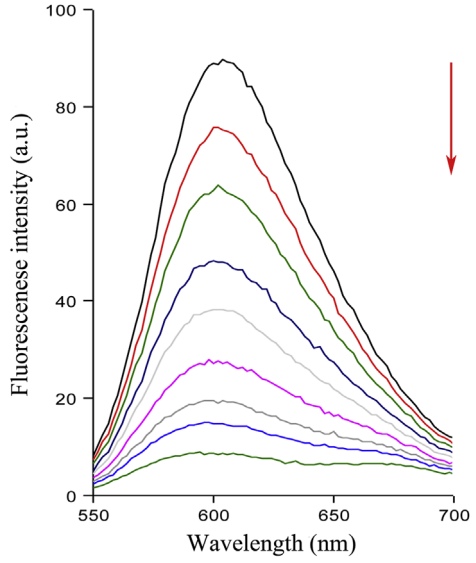

Figure 6 Fluorescence emission spectra (λ_{ex} = 530 nm) of the CT-DNA-ethidium bromide ($C_{DNA} = 4.8 \times 10^{-5}$ mol/L) in the presence of increasing amounts of EB (0, 1.2×10^{-6}, 2.6×10^{-6}, 4.3×10^{-6}, 6.0×10^{-6}, 8.4×10^{-6}, 1.0×10^{-5}, 1.3×10^{-5}, 1.6×10^{-5} mol/L). Arrows show the changes in fluorescence intensity with respect to an increase in the concentration.

concentration of EB increased, the fluorescence intensity was largely decreased. Such a characteristic change ($K_{sv} = 5.08 \times 10^5$ L/(mol/L)) is often observed in the typical intercalative interaction between compounds and DNA. The maximum UV–vis absorption wavelength of the EB occurs in 608 nm. With the addition of CT-DNA, the above bands corresponding to EB showed significant hypochromism accompanied with a red shift, indicating the intercalative interaction between EB and CT-DNA. The UV–vis titration curves were showed in Supplementary information Fig. S4.

3.10. Self-blocking experiment

As shown in Fig. 7a, excessive cold EB significantly reduced the uptake of ^{131}I-EB in necrotic muscle (0.47 ± 0.07%ID/g) compared to the non-blocking group (1.35 ± 0.22%ID/g) ($P < 0.01$), which indicated that about 65% of the radioactivity was blocked by EB. The results were further confirmed by autoradiography and corresponding H&E staining in Fig. 7b. Autoradiography showed that high ^{131}I-EB uptake appeared only in the necrotic parts (pink colored on H&E images staining), which was consisted with the results of biodistribution. This suggests that ^{131}I-EB and cold EB may have the same specific targets of necrotic tissues.

4. Discussion

In the present study, we investigated the necrosis avidity of EB in search for candidates with necrosis targetability from clinical medicines. The results indicated that ^{131}I-EB could specifically bind to necrotic tissues and image necrosis in living animals. Furthermore, the necrosis targeting mechanism of EB might be attributed to its binding ability with exposed DNA in necrotic tissues.

Necrosis avidity of ^{131}I-EB was corroborated at the cellular and whole animal level. The *in vitro* cells binding assays demonstrated that the uptake of ^{131}I-EB in necrotic cells was higher than that in viable cells. Comparison of *ex vivo* autoradiography with corresponding H&E staining indicated that the uptakes of ^{131}I-EB in the infarcted liver lobe and necrotic muscle were much higher than that in the non-infarcted liver lobe and normal muscle, respectively. These findings are consistent with that of tissue γ courting. Moreover, both the co-localization of fluoromicroscopic images and corresponding H&E staining confirmed that the red fluorescence of ^{131}I-EB was mainly located in the necrotic tissues. All the above results proved that ^{131}I-EB has avidity for necrotic tissue.

The mechanism that EB targets the necrotic tissues may be due to its binding ability with exposed DNA in the necrotic tissues. Cell necrosis enables the disruption of the cell membrane and the

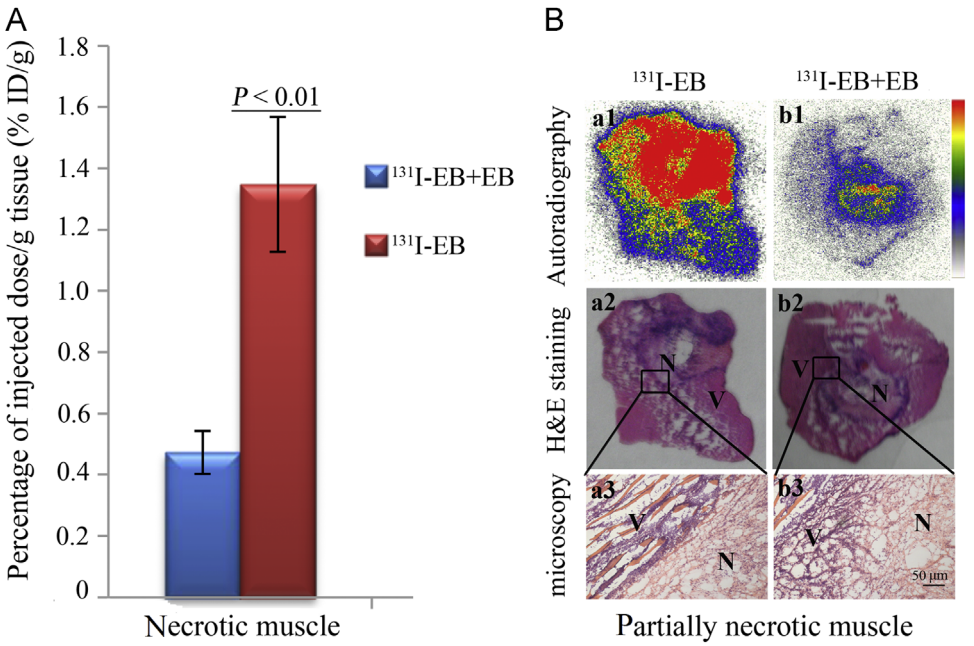

Figure 7 ^{131}I-EB (14.8 MBq/kg, 2 mg/kg) was blocked by excessive EB (10 mg/kg) in necrotic muscle model rats. (A) Uptake of ^{131}I-EB in no-blocked and 10 mg/kg EB blocked necrotic muscle. The results are presented as %ID/g 24 h after coinjection ($P<0.01$). (B) Autoradiograms (upper panels), corresponding H&E images (middle panels), and micrograph (lower panels) of partially necrotic muscle sections. No-blocked (^{131}I-EB) partially necrotic muscle (a1–a3); 10 mg/kg EB (^{131}I-EB+EB) blocked partially necrotic muscle (b1–b3). ($n = 6$, Scale bar=50 μm).

release of the cellular contents, *e.g.*, genomic DNA[32], which become the targets for NAAs. Previous studies have demonstrated that the planar-structured compounds have the potential ability to intercalate into double stranded DNA by forming stable complexes[32–34]. Considering that EB is a nearly planar compound which consists of two azo-naphthalene-disulfonates, it may have the ability to interact with DNA. Our present study showed that the binding constant of EB with CT-DNA was 5.08×10^5 L/(mol/L), which was 400 times more than that of 2-aminoanthraquin (1.25×10^3 L/(mol/L)), a well-known DNA intercalating agent[35]. This demonstrated that EB has strong binding affinity toward DNA. We further applied the UV–vis spectroscopy experiment to confirm that EB could bind to DNA by intercalate mode. Cell nuclear extraction and fluorescence microscopy experiments demonstrated that EB was mainly located in the nuclear region of necrotic cells. Taken together, it can be deduced that EB can accumulate in necrotic tissues probably by binding with exposed DNA.

In previous study, EB has been found to bind to the serum albumin and form macromolecular compounds, which inhibits its passage into living cells or across the blood vessel[18]. Therefore, EB was applied to assess the integrity of the blood–brain barrier or vascular permeability in clinical applications[36]. We herein demonstrated that EB could target to the necrotic tissues by binding to the exposed DNA for the first time, suggesting EB has a potential application for imaging of necrosis related diseases or tumor therapy if labeled by corresponding radionuclide.

Exposed DNA released from the necrotic tissues is an ideal, specific and stable target for necrosis imaging and tumor therapy. Generally, the intracellular DNA concentration is in the millimolar range, therefore high concentrations of DNA are probably produced in the extracellular space of tissue with high levels of necrosis[26]. At the same time, the DNA chain contains a large number of base pairs, which could provide rich binding sites for DNA intercalators such as EB and ethidium bromide[37]. Although sometimes DNA can be detected in the blood under pathological conditions, the concentration of DNA in the blood is still significantly lower than in necrotic tissue because of the presence of serum nucleases and the large blood volume[26].

Currently, the majority of radiopharmaceuticals are designed to bind to the receptors or antigens overexpressed on the viable tumor cells. However, tumor heterogeneity leads to inhomogeneous distribution of targeted drugs in tumor, which reduces the uptake and limits the treatment effectiveness of the medication[38]. Since spontaneous necrosis or necrosis induced by antineoplastic drugs always appears in the tumors, the exposed DNA in necrotic tumor becomes a more stable and generic target with less heterogeneity and drug resistance[39]. Accordingly, better diagnosis and curative effect can be achieved by the drugs targeting to the exposed DNA.

As a highly water-soluble and safe necrosis avid compound, ^{131}I-EB would have potential clinical applications in imaging necrosis. ^{131}I-EB can be dissolved in PBS or saline for intravenous injection in animals and humans. In contrast, most NAAs including ^{131}I-hypericin[6] and ^{131}I-sennidin A[40] are water-insoluble and must be dissolved in organic solvents such as dimethylsulfoxide (DMSO). However, DMSO as a genotoxic solvent is not suitable for clinical applications[17]. What's more, EB has been used to determine the total blood volume in clinical without any adverse reactions, even in pregnant women and newborn babies[41,42].

Intense color of EB could be used for precise boundary delineation of the necrotic lesions, which is crucial for clinical diagnosis and surgical treatment. For example, EB staining might help to make a clear-cut distinction of pancreatic necrosis and normal tissue during the operation of pancreatitis, which would be helpful for guiding the doctor to completely remove the necrotic tissues to achieve the therapeutic purpose. In contrast, if the necrotic pancreas could not be completely resected in surgery, it would eventually cause further deterioration of the pancreas and

fatal danger[43]. Similarly, as a low-cost, technically simple and reliable staining method, EB staining may be applied to delineate and obtain the necrotic tissue sample in animal experiments.

Although ^{131}I-EB can specifically bind to necrotic tissues, there are some problems need to be solved such as its high accumulation in normal liver. Intense hepatic uptake may affect the imaging quality of abdomen disease (*e.g.*, pancreatic necrosis) and heart disease (*e.g.*, myocardial infarction)[29]. At the same time, high doses of ^{131}I-EB in the liver will cause radiation damage, which was demonstrated by short- and long-term clinical observation[44]. The high accumulation of ^{131}I-EB in liver may be attributed to its π-conjugated planar structure, which has the tendency to form aggregates in aqueous environment[45] and retention in the MPS. In addition, previous study indicated that compounds with excess negative charge mainly accumulated in the liver after injection[46], indicating that the negative charge of EB may also play a role in biodistribution. Accordingly, reducing the uptake of EB in the liver could be a starting point for further research.

Acknowledgments

This work was partially supported by the National Natural Science Foundation of China (Nos. 81501536 and 81473120), A Project Funded by the Priority Academic Program Development of Jiangsu Higher Education Institutions and the Open Project Program of Jiangsu Key Laboratory of Drug Screening (No. JKLDS2015KF-02).

Appendix A. Supplementary material

Supplementary data associated with this article can be found in the online version at http://dx.doi.org/10.1016/j.apsb.2017.08.002.

References

1. Smith BA, Smith BD. Biomarkers and molecular probes for cell death imaging and targeted therapeutics. *Bioconjugate Chem* 2012;**23**:1989–2006.
2. De Saint-Hubert M, Prinsen K, Mortelmans L, Verbruggen A, Mottaghy FM. Molecular imaging of cell death. *Methods* 2009;**48**:178–87.
3. Edinger AL, Thompson CB. Death by design: apoptosis, necrosis and autophagy. *Curr Opin Cell Biol* 2004;**16**:663–9.
4. Eguchi A, Wree A, Feldstein AE. Biomarkers of liver cell death. *J Hepatol* 2014;**60**:1063–74.
5. Dean E, Greystoke A, Ranson M, Dive C. Biomarkers of cell death applicable to early clinical trials. *Exp Cell Res* 2012;**318**:1252–9.
6. Ni YC, Huyghe D, Verbeke K, De Witte PA, Nuyts J, Mortelmans L, et al. First preclinical evaluation of mono-[^{123}I] iodohypericin as a necrosis-avid tracer agent. *Eur J Nucl Med Mol Imag* 2006;**33**:595–601.
7. Marvsael T, Putte MV, Fonge H, Cona MM, Li JJ, Bormans G, et al. Radiolabeled iodohypericin as tumor necrosis avid tracer: diagnostic and therapeutic potential. *Int J Cancer* 2012;**131**:129–37.
8. Ni YC, Bormans G, Chen F, Verbruggen A, Marchal G. Necrosis avid contrast agents: functional similarity *versus* structural diversity. *Investig Radiol* 2005;**40**:526–35.
9. Fonge H, Chitneni SK, Jin LX, Vunckx K, Prinsen K, Nuyts J, et al. Necrosis avidity of ^{99m}Tc(CO)$_3$-labeled pamoic acid derivatives: synthesis and preliminary biological evaluation in animal models of necrosis. *Bioconjugate Chem* 2007;**18**:1924–34.
10. Wang H, Sun X, Chen F, De Keyzer F, Yu J, Landuyt W, et al. Treatment of rodent liver tumor with combretastatin A4 phosphate: noninvasive therapeutic evaluation using multiparametric magnetic resonance imaging in correlation with microangiography and histology. *Investig Radiol* 2009;**44**:44–53.
11. Delmonte A, Sessa C. AVE8062: a new combretastatin derivative vascular disrupting agent. *Exp Opin Investig Drug* 2009;**18**:1541–8.
12. Li JJ, Sun ZP, Zhang J, Shao HB, Cona MM, Wang HJ, et al. A dual-targeting anticancer approach: soil and seed principle. *Radiology* 2011;**260**:799–807.
13. Shao HB, Ni YC, Dai X, Zhang J, Chen F, Fan GG, et al. Diffusion-weighted MR imaging allows monitoring the effect of combretastatin A4 phosphate on rabbit implanted VX2 tumor model: 12-day dynamic results. *Eur J Radiol* 2011;**81**:578–83.
14. Jeong AK, Sang IC, Dong HK, Park SB, Lee SS, Choi SN, et al. Evaluation by contrast-enhanced MR imaging of the lateral border zone in reperfused myocardial infarction in a cat model. *Korean J Radiol* 2000;**2**:21–7.
15. Lund GK, Higgins CB, Wendland MF, Watzinger N, Weinmann HJ, Saeed M. Assessment of nicorandil therapy in ischemic myocardial injury by using contrast-enhanced and functional MR imaging. *Radiology* 2001;**221**:676–82.
16. Ni YC, Cresens E, Adriaens P, Miao Y, Verbeke K, Dymarkowski S, et al. Necrosis-avid contrast agents: introducing nonporphyrin species. *Acad Radiol* 2002;**9**:98–101.
17. Van DPM, Roskams T, Bormans G, Verbruggen A, De Witte PA. The impact of aggregation on the biodistribution of hypericin. *Int J Oncol* 2006;**28**:655–60.
18. Cooksey C. Quirks of dye nomenclature. 1. Evans blue. *Biotech Histochem* 2014;**89**:111–3.
19. Oskar SW, Igor K. Selective vulnerability of the blood–brain barrier in chemically induced lesions. *J Neuropathol Exp Neurol* 1996;**25**:542–59.
20. Young TE, Gallie DR, Demason DA. Ethylene-mediated programmed cell death during maize endosperm development of wild-type and shrunken2 genotypes. *Plant Physiol* 1997;**115**:737–51.
21. Atkinson MM, Keppler LD, Orlandi EW, Baker JC, Mischiefs CF. Involvement of plasma membrane calcium influx in bacterial induction of the K^+/H^+ and hypersensitive responses in tobacco. *Plant Physiol* 1990;**92**:215–21.
22. Baker CJ, Mock NM. An improved method for monitoring cell death in cell suspension and leaf disc assays using evans blue. *Plant Cell Tissue Org Cult* 1994;**39**:7–12.
23. Leist M, Nicotera P. 28–Cell death: apoptosis versus necrosis. In: KMA Welch, Caplan LR, Reis DJ, Bo KS, Weir B, editors. *Primer on Cerebrovascular Disease*. 2rd ed. Philadelphia: Academic Press; 1997. p. 101–4.
24. Farquhar WB, Hunt BE, Taylor JA, Darling SE, Freeman R. Blood volume and its relation to peak O_2 consumption and physical activity in patients with chronic fatigue. *Am J Physiol Heart Circ Physiol* 2002;**282**:66–71.
25. Scoon GS, Hopkins WG, Mayhew S, Cotter JD. Effect of post-exercise sauna bathing on the endurance performance of competitive male runners. *J Sci Med Sport* 2007;**10**:259–62.
26. Dasari M, Lee S, Sy J, Kim D, Lee S, Brown M, et al. Hoechst-IR: an imaging agent that detects necrotic tissue *in vivo* by binding extracellular DNA. *Org Lett* 2010;**12**:3300–3.
27. Ragazzon PA, Iley J, Missailidis S. Structure-activity studies of the binding of the flavonoid scaffold to DNA. *Anticancer Res* 2009;**29**:2285–93.
28. Cona MM, Koole M, Feng YB, Liu Y, Verbruggen A, Oyen R, et al. Biodistribution and radiation dosimetry of radioiodinated hypericin as a cancer therapeutic. *Int J Oncol* 2014;**44**:819–29.
29. Flotats A, Carrió I. Non-invasive *in vivo* imaging of myocardial apoptosis and necrosis. *Eur J Nucl Med Mol Imaging* 2003;**30**:615–30.
30. Reichmann ME, Rice SA, Thomas CA, Doty P. A further examination of the molecular weight and size of desoxypentose nucleic acid. *J Am Chem Soc* 1954;**76**:3047–53.
31. Lepecq JB, Paoletti C. A fluorescent complex between ethidium bromide and nucleic acids physical-chemical characterization. *J Mol Biol* 1967;**27**:87–106.

32. Kressel M, Groscurth P. Distinction of apoptotic and necrotic cell death by *in situ* labelling of fragmented DNA. *Cell Tissue Res* 1994;**278**:549–56.
33. Bischoff G, Hoffmann S. DNA-binding of drugs used in medicinal therapies. *Curr Med Chem* 2002;**9**:312–48.
34. Strekowski L, Wilson B. Noncovalent interactions with DNA: an overview. *Mutat Res* 2007;**623**:3–13.
35. Yang HX, Song W, Jing MY, Liu R. Study on the interaction mechanism of 2-aminoanthraquinone with calf thymus DNA. *J Biochem Mol Toxicol* 2013;**27**:272–8.
36. Valle JD, Camins A, Pallàs M, Vilaplana J, Pelegríc C. A new method for determining blood–brain barrier integrity based on intracardiac perfusion of an evans blue–hoechst cocktail. *J Neurosci Methods* 2008;**174**:42–9.
37. Apalkov V, Berashevich J, Chakraborty T. Unique magnetic signatures of mismatched base pairs in DNA. *J Chem Phys* 2010;**132**:085102.
38. Huang M, Shen AJ, Ding J, Geng MY. Molecularly targeted cancer therapy: some lessons from the past decade. *Trends Pharmacol Sci* 2014;**35**:41–50.
39. Li JJ, Chen F, Cona MM, Feng YB, Himmelreich U, Oyen R, et al. A review on various targeted anticancer therapies. *Target Oncol* 2012;**7**:69–85.
40. Wang JH, Jiang CH, Jiang X, Li Y, Zhang J, Sun ZP, et al. The research on biodistribution of ~^{131}I-iodosennoside a in normal mice and to evaluate myocardial activity. *J Isot* 2013;**26**:98–103.
41. Gibson JG, Evans WA. Clinical studies of the blood volume. I. Clinical application of a method employing the azo dye "evans blue" and the spectrophotometer. *J Clin Investig* 1937;**16**:301–16.
42. Linderkamp O, Mader T, Butenandt O, Riegel KP. Plasma volume estimation in severely ill infants and children using a simplified evans blue method. *Eur J Pediatr* 1977;**125**:135–41.
43. Kulkarni S, Bogart A, Buxbaum J, Matsuoka L. Surgical transgastric debridement of walled off pancreatic necrosis: an option for patients with necrotizing pancreatitis. *Surg Endosc* 2015;**29**:575–82.
44. Bohuslavizki KH, Klutmann S, Brenner W, Mester J, Henze E, Clausen M. Salivary gland protection by amifostine in high-dose radioiodine treatment: results of a double-blind placebo-controlled study. *J Clin Oncol* 1998;**16**:3542–9.
45. Frid P, Anisimov SV, Popovic N. Congo red and protein aggregation in neurodegenerative diseases. *Brain Res Rev* 2007;**53**:135–60.
46. Liu XJ, Jiang CH, Yue L, Liu W, Yao N, Gao M, et al. Evaluation of hypericin: effect of aggregation on targeting biodistribution. *J Pharm Sci* 2015;**104**:215–22.